*Article*

# Effect of Cu Additions on the Evolution of Eta-prime Precipitates in Aged AA 7075 Al–Zn–Mg–Cu Alloys

Ting-Jung Hsiao [1], Po-Han Chiu [1,*], Cheng-Lin Tai [1], Tzu-Ching Tsao [1], Chien-Yu Tseng [1], Yi-Xian Lin [1], Hsueh-Ren Chen [1], Tsai-Fu Chung [2], Chih-Yuan Chen [3], Shing-Hoa Wang [4] and Jer-Ren Yang [1,*]

[1] Department of Materials Science and Engineering, National Taiwan University, Taipei 10617, Taiwan
[2] Department of Materials Science and Engineering, National Yang Ming Chiao Tung University, Hsinchu 30010, Taiwan
[3] Graduate Institute of Intellectual Property, National Taipei University of Technology, Taipei 10608, Taiwan
[4] Department of Mechanical Engineering, National Taiwan Ocean University, Keelung 20224, Taiwan
* Correspondence: tedchiu20@gmail.com (P.-H.C.); jryang@ntu.edu.tw (J.-R.Y.)

**Abstract:** In the present study, after solid solution treatment, four different artificial aging treatments (100, 120, 140 and 160 °C) were performed on Al-5.98Zn-2.86Mg-1.61Cu (wt.%) alloy, denoted as 7075-LCu, and Al-5.91Zn-2.83Mg-1.98Cu (wt.%) alloy, denoted as 7075-HCu. Peak aging conditions were determined for each aging temperature at various hold time intervals of up to 24 h. It was found that both alloys possessed the optimal strengths after artificial aging at 120 °C for 24 h. Under this condition, the ultimate tensile strengths (UTSs) were 618 MPa (7075-LCu) and 623 MPa (7075-HCu), respectively. Moreover, a method was used to calculate the average sizes and number density of the major strengthening precipitates, $\eta'$, under peak aging conditions in these two alloys from transmission electron microscopy (TEM) images and electron energy loss spectroscopy (EELS). The above results indicated that for the 7075-LCu and 7075-HCu samples with the optimal UTS strengths, the former possessed an average thickness of 2.15 nm, and a number density of $3.27 \times 10^{17}$ cm$^{-3}$; the latter, 2.04 nm and $3.52 \times 10^{17}$ cm$^{-3}$.

**Keywords:** Al-Zn-Mg-Cu alloys; artificial aging; $\eta'$ precipitates; crystallography; HR-TEM; HAADF/STEM; EELS; nano-particle size measurement

## 1. Introduction

Al-Zn-Mg-Cu alloys are widely used in the aerospace and automobile industries. The precipitation hardening mechanism provides the alloys with outstanding strength relative to that of other aluminum alloys. The sequence of the evolution of the precipitates is as follows: super-saturated solid solution (SSSS) → GP zones (GP I and II) → $\eta'$ precipitates → $\eta$ [1,2]. Generally, $\eta'$ precipitates are considered the major strengthening phase after T6 heat treatment [2,3]. The size of the $\eta'$ precipitates, which are usually only a few nanometers thick, is a decisive factor affecting the strength of the alloys [3]. Thus, it is valuable to understand the relationship between the sizes of $\eta'$ precipitates and their mechanical properties.

To determine the peak aging for different aging treatments, previous works [4–7] investigating Al-Zn-Mg-Cu alloys have widely applied hardness tests. Moreover, some previous works [4,7] have further implemented tensile tests to obtain mechanical properties such as yield strength (YS), ultimate tensile strength (UTS), and elongation at peak aging. It is well known that the sizes of the precipitates in Al-Zn-Mg-Cu alloys are closely related to the mechanical properties, such as the hardness, strength, and elongation [3,6,8,9]. Previous studies [3,10] have attempted to relate the sizes of precipitates to different aging treatments. In the present work, we employed four different artificial aging temperatures coupled with holding times of 0–24 h to identify the peak aging conditions. Then, in the peak

aging conditions, the sizes of the precipitates were measured and the mechanical properties were examined.

To investigate the sizes of precipitates, various methods, such as small angle X-ray scattering (SAXS), atom probe tomography (APT) and transmission electron microscopy (TEM), are applied. SAXS is superior to the others for obtaining average data on a large scale (10 mm × 10 mm) but even so η′ precipitates cannot be directly observed by this method. However, the average size and the number density of η′ were evaluated by a fitting model [10,11]. It is presumed that the data of fitting curves are affected by various types and sizes of the precipitates in Al-Zn-Mg-Cu alloys after aging treatments. Generally, SAXS is suitable when there are no more than two types of particles. In Al-Zn-Mg-Cu alloys after aging treatments, however, there are more than two types of precipitates or solute clusters on the nanoscale. These precipitates may include unknown solute clusters (such as precursors of GPI and GPII zones); GPI and GPII zones; η′, η, and T ($Mg_{32}(Al, Zn)_{49}$) phases; and $Al_3Zr$ dispersoids [12]. Thus, the presence of multiple kinds of precipitates on the same scale as η′ may limit the precision of SAXS. In contrast, APT is considered to be more useful for identifying the chemical compositions of precipitates [2,13,14]. Nonetheless, the scale of single APT processing is relatively small (50 nm × 50 nm × 500 nm) and the collection efficiency is limited. Finally, TEM images for collecting data on η′ cover an area slightly larger than 200 nm × 200 nm. Though the coverage of a single image may not be sufficiently large to reflect the whole sample, multiple TEM images can be captured and analyzed to reduce the potential bias caused by a single image. In TEM images, η′ has been characterized by the morphology [2,3,15,16] and by the orientation relationship (OR) between the η′ precipitate and the Al matrix [17]; the latter (OR) can be obtained from high-resolution TEM (HR-TEM) images with Fast Fourier Transform (FFT) diffractograms [17]. Compared with SAXS and APT, TEM imaging is presumably more prevalent and accessible for researchers. Thus, the TEM method is likely to be employed extensively in the related research works.

The use of TEM images to develop data on nanoscale precipitates in aluminum alloys is not a new approach. Previous research has applied TEM images to reveal the different kinds of precipitates by morphology and to measure the average sizes of the precipitates [3,6,9,14,18]. Nevertheless, most studies have not provided clear standards for identifying the η′ precipitates. Some previous works [19,20] have asserted that η′ precipitates are plate-like. However, in one previous work [21], η′ precipitates observed along the $[110]_{Al}$ zone axis were only considered to be rod-like, without other possible morphologies. Such observations led to incorrect results, for η′ precipitates can vary greatly in morphology, appearing as ellipses even along the same $[110]_{Al}$ zone axis, depending on whether the precipitate is edge-on or not [17]. In some previous works [8,9], the concept of the equivalent circle radius (ECR) has been used for measuring the sizes of the η′ precipitates without distinguishing edge-on η′ precipitates from non-edge-on η′ precipitates. A major concern is that this application could lead to some bias, as edge-on η′ precipitates present the thickness of η′ plates, whereas non-edge-on η′ precipitates present an oval shape due to projection. To interpret this phenomenon, crystallography and orientation relationships disclose that there should always be two kinds of morphologies of η′ precipitates in the aluminum matrix when observed along the $[110]_{Al}$ zone axis; the edge-on η′ precipitates resemble thick lines, and their non-edge-on counterparts appear as ellipses. Moreover, in a previous study [6], only a portion of the precipitates in the TEM images was recognized and counted. We believe that this condition can be improved by combining TEM images and software to reduce the potential bias. In the present work, we aimed to establish a procedure for analyzing most of the precipitates in AA7075 alloys by using nanoscale TEM images. Knowledge of crystallography and morphology and software of accessible image-processing were applied in the analysis to determine the size of precipitates.

On the other hand, another previous work [10] that studied Al-6.56Zn-2.25Mg-2.10Cu-0.12Zr (wt.%) with TEM and SAXS has indicated that both size and number density of

precipitates have been the two critical factors for the strength of aluminum alloys after artificial aging. To investigate the size and number density of nanoscale precipitates, other previous works [22,23] demonstrated the investigation of the number density of nanoparticles in alloys by TEM equipped with EELS, which was applied to measure the thickness of specimens. For example, a previous study [22] investigated the number density of carbides in the Fe-9/10Cr (wt.%) ferritic alloys. Moreover, another previous work [23] measured the number density of Cu-rich precipitates in Fe–C–Ni–Mn–Si alloys. In the present work for estimating both the size and number density of η′ precipitates in the aluminum alloys, TEM imaging coupled with EELS was carried out, instead of SAXS. The TEM observation areas' thicknesses were determined via the analysis of EELS.

A previous study [24] on Al-7.8Zn-1.6Mg-xCu-0.14Zr alloys (x = 0, 0.8, 1.6 wt.%) found that both the tensile strength and elongation increase as the Cu content increases as the sample was treated at 120 °C for 24 h. That the elongation can be significantly improved by adding Cu in these alloys is worth noting. In contrast, another work [25] on Al-9.3Zn-2.4Mg-xCu-0.16Zr alloys (x = 0.8, 1.3, 1.5, 1.8, and 2.2 wt.%) employed the same aging condition (at 120 °C for 24 h) and demonstrated inverse trends between tensile strength and elongation; the results indicated that, as the Cu content increased, the YS and UTS fell, while the elongation increased. As compared between these two previous works [24,25], the effect of the addition of Cu on the mechanical properties could not be elucidated. Regarding the influence of Cu on η′ and η precipitates, another work [26] suggested that the addition of Cu is vital to retarding the phase transformation from η′ to η and to deterring the coarsening of η. Nevertheless, this viewpoint has not been further supported by later research works. Recently, a study on Al-8.9Zn-2.15Mg-2.05Cu-0.14Zr-0.02Sc (wt.%) alloy [27] observed the segregation of Cu at the boundaries around η, detected by the energy-dispersive X-ray spectroscopy (EDS) mapping of η. However, this study did not provide further conclusions about whether the addition of Cu can refine the size of η′. The addition of Cu to Al-Zn-Mg alloys has a significant effect on the mechanical properties, but the effect on the η′ precipitate size is unclear.

The present work aimed to investigate the precipitation evolution at different peak aging conditions in two AA7075 alloys with different contents of Cu (1.61 and 1.98 wt.%). After the solution treatment, four different artificial aging treatments (100, 120, 140, and 160 °C) at different hold time intervals of up to 24 h were performed. The peak aging conditions for four aging temperatures were determined by data from Vickers hardness measurements and tensile tests. To evaluate the effect of different Cu contents on η′ precipitates, a method of characterizing the η′ precipitates was developed and applied. To more accurately identify the precipitates, the method first exploits current knowledge of crystallography and the relationship of crystal orientation to morphology. In order to provide more valid and objective data, in our method, the TEM images show a clear contrast between η′ and Al matrix, so firstly the precipitates can be clearly discerned, and secondly, most of the precipitates can be counted. Furthermore, to estimate the number density of the η′ precipitates, the thicknesses of specimens were measured by EELS. Finally, the mechanical properties are linked to the size and number density of η′ precipitates.

## 2. Materials and Methods

The materials used in this study were the Al-5.98Zn-2.86Mg-1.61Cu and Al-5.91Zn-2.83Mg-1.98Cu (wt.%) alloys; the former alloy is denoted as 7075-LCu and the latter is denoted as 7075-HCu. The alloys were provided by the China Steel Corporation (Kaohsiung, Taiwan). Before receipt, the samples had been rolled and sliced into A4 sheets of 3 mm thickness. Then the samples were subjected to the following heat treatments: (i) supersaturated solid solution treatment at 490 °C, holding for 30 min, (ii) natural aging at 25 °C for 7 days, and (iii) artificial aging at 100, 120, 140 and 160 °C, respectively, for 2–24 h. Vickers hardness measurements were performed by a microhardness tester (FM-700, Future-Tech Corp., Kawasaki, Kanagawa, Japan) with an applied load of 500 g and a dwelling time of 8 s. Hardness data were obtained from the average of more than 15 measurements with

the corresponding standard deviation. Samples for tensile tests were prepared according to the ASTM E8 standard. Tensile tests were executed by MTS Landmark (Eden Prairie, MN, USA) Dynamic Test System with a strain rate of $1.0 \times 10^{-3}$ s$^{-1}$ at room temperature, and the strains were measured by laser. Finally, the peak aging (PA) conditions for the different specimens were determined. Specimens for TEM were prepared by slicing pieces from selected samples and then thinning them to 0.06 mm. The thinned specimens were subsequently twin-jet electropolished at around $-25\,^{\circ}$C in a solution of 30% nitric acid and 70% methanol with a working voltage range of 12–15 V. Afterward, the TEM specimens were observed with a field-emission-gun TEM (FEI Tecnai G2 F20, Thermo Fisher Scientific, Waltham, MA, USA), operating at 200kV. The nano-sized precipitates were examined in TEM images, and their sizes were further measured with the open-access software Fiji 4.1 [28]. Fast Fourier Transform (FFT) diffractograms of the η′ phase were obtained from the HR-TEM images and compared with the simulated diffraction patterns. The lattice parameters used to simulate the diffraction patterns of η′ phase were $a$ = 0.504 nm and $c$ = 1.303 nm [29]. STEM/EDX mappings were obtained with a field-emission-gun TEM (FEI Talos F200X G2, Thermo Fisher Scientific, Waltham, MA, USA). Specimen thickness was measured by a field-emission-gun TEM (FEI Tecnai G2 F30, Thermo Fisher Scientific, Waltham, MA, USA) equipped with electron energy loss spectroscopy (EELS) by the log-ratio method [30–32], which was operated at 300 kV in TEM mode and collected with a semi-collection angle of 19.36 mrad. The mean free path in the studied aluminum alloys applied in this study was 178 nm for plasma oscillation.

　　The crystallography and orientation relationships between η′ and the Al matrix are elucidated below [17]. η′ has already been proved to grow on its habit plane, {111}$_{Al}$, and the four variants of η′ and their orientation relationships with the Al matrix are listed in Table 1. From Table 1 and Figure 1a, we can realize that under no conditions would all the η′ be in the edge-on configuration. Along the [110]$_{Al}$ zone axis, for example, only two of the four η′ variants can be edge-on; the other two variants of η′ would be projected as ellipses in the TEM images. In Figure 1c, since η′ is a plate-like precipitate in the TEM images, the edge-on η′ shows the thickness of the plate, denoted as t in Figure 1b. The two edge-on conditions, labeled η$_1$′ and η$_2$′ in Figure 1c, possess a specific orientation relationship. Under the observation along the [110]$_{Al}$ zone axis, the included angle of these two edge-on η′ precipitates is 70.52°. On the other hand, the η′ precipitates that are not edge-on, labeled η$_3$′ and η$_4$′ in Figure 1c, show the areas of the circular plates, which are presented as ellipses due to the projection. These ellipses cannot directly present the actual size of the plate-like η′; however, their true areas can be estimated by dividing by the projection factor. The projection factor is the cosine of the dihedral angle, 35.26°, between (110)$_{Al}$ and (111)$_{Al}$, and the value of the projection factor is 0.816. η$_3$′ and η$_4$′ cannot be discriminated from each other by their morphology or orientation relationship due to the projection of [110]$_{Al}$.

**Table 1.** Four variants of η′ precipitates.

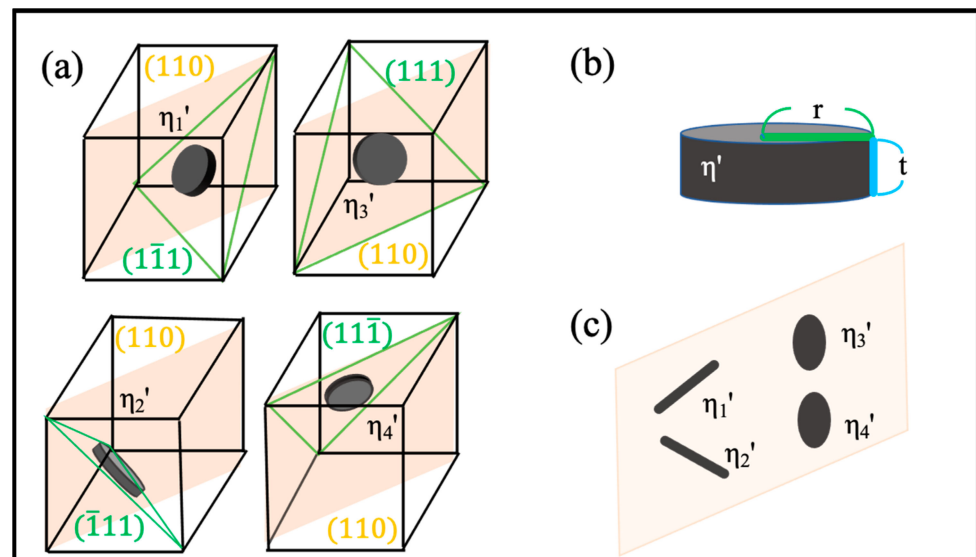| η′ | Orientation Relationship | |
|---|---|---|
| 1 | $(0001)\eta'\,//\,(1\bar{1}1)_{Al}$ | $[10\bar{1}0]_{\eta'}\,//\,[110]_{Al}$ |
| 2 | $(0001)\,\eta'\,//\,(\bar{1}11)_{Al}$ | $[10\bar{1}0]_{\eta'}\,//\,[110]_{Al}$ |
| 3 | $(0001)\eta'\,//\,(111)_{Al}$ | $[10\bar{1}0]_{\eta'}\,//\,[\bar{1}10]_{Al}$ |
| 4 | $(0001)\,\eta'\,//\,(11\bar{1})_{Al}$ | $[10\bar{1}0]_{\eta'}\,//\,[\bar{1}10]_{Al}$ |

**Figure 1.** Illustration of orientation relationships of four variants of η′: (**a**) η′ (in blue) on the {111}$_{Al}$ habit planes, with the observed (110)$_{Al}$ planes in orange; (**b**) the presumed circular plate-like morphology of η′ (the thickness denoted as t, and the radius, r); (**c**) along the [110]$_{Al}$ zone axis, two of the η′ being edge on (appearing as thick lines), and the other two η′ being distorted (appearing as ellipses).

## 3. Results and Discussion

### 3.1. Peak Aging (PA) Condition

Hardness tests were implemented to determine the PA conditions for artificial aging at different temperatures. The results are presented in Figure 2. Tensile tests were further carried out to confirm the results of the hardness tests. We found that, for most conditions, the PA conditions of 7075-LCu samples were the same as those of 7075-HCu samples; for the aging temperatures of 100 °C, 120 °C, 140 °C, and 160 °C, the PA times were 22, 24, 10, and 14 h, respectively. For 7075-LCu samples at 140 °C, the results of hardness tests showed the hardness was slightly (1 HV) higher after 14 h than after 10 h. However, the tensile tests suggested that the strength of 7075-LCu samples aged at 140 °C for 10 h was higher than that of samples aged for 14 h. Thus, we set a PA condition for 7075-LCu at 140 °C and 10 h. The trends of aging hardness exhibited fluctuations. These fluctuations have been presumed to indicate "hardness reversion" [33], which is probably caused by the dynamic solution and precipitates during the aging process. It is generally believed that during artificial aging, some existing precipitates dissolve back into the aluminum matrix, some precipitates grow, and new precipitates are dynamically formed [34].
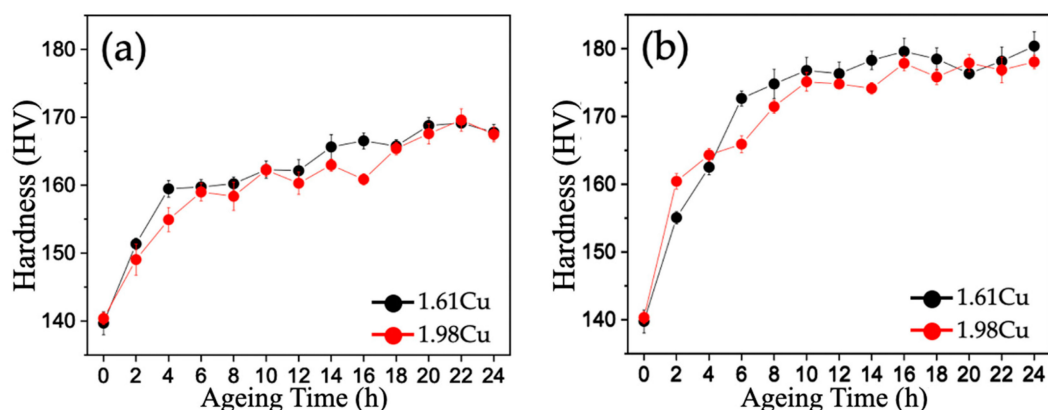


**Figure 2.** *Cont.*
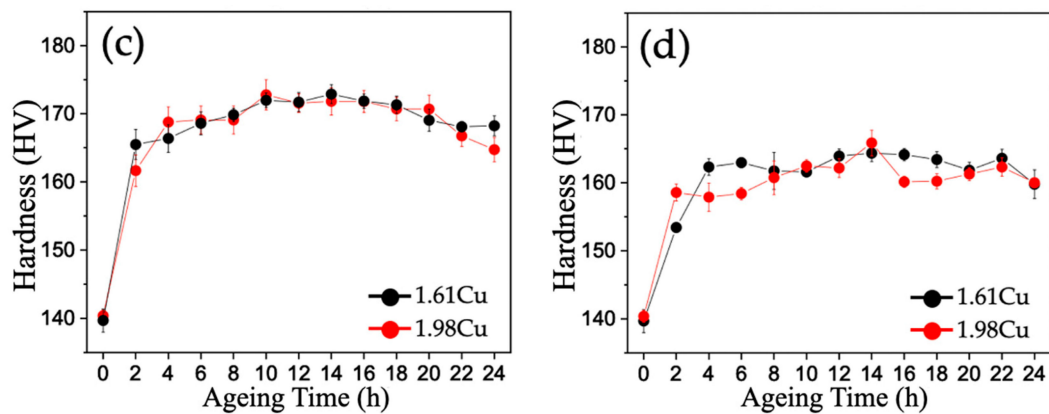
**Figure 2.** Hardness tests after artificial aging treatments at (**a**) 100 °C, (**b**) 120 °C, (**c**) 140 °C, and (**d**) 160 °C.

### 3.2. Mechanical Properties

The stress-strain curves of the two alloys subjected to the PA conditions, respectively at 100, 120 140, and 160 °C are shown in Figure 3. At least three specimens of each aging condition were employed for the corresponding tensile test. The yield stress (YS), ultimate tensile stress (UTS), and total elongation for each condition are summarized in Tables 2 and 3. The PA conditions determined by the hardness tests were confirmed by the tensile tests.
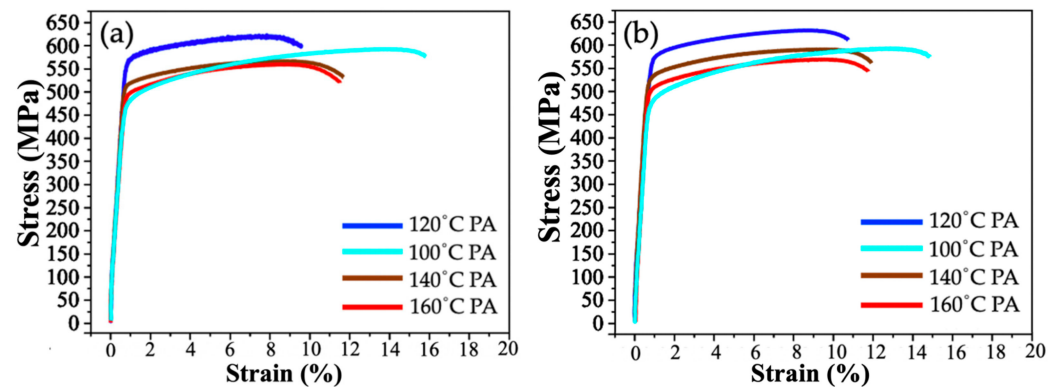


**Figure 3.** Stress-strain curves for (**a**) 7075-LCu and (**b**) 7075-HCu subjected to different PA treatments.

**Table 2.** Mechanical properties of 7075-LCu subjected to different PA treatments.

| Aging Temp. | YS (MPa) | UTS (MPa) | Total Elongation (%) |
|---|---|---|---|
| 100 °C | 451 ± 3 | 595 ± 2 | 14.0 ± 1.7 |
| 120 °C | 553 ± 5 | 618 ± 3 | 11.0 ± 1.4 |
| 140 °C | 496 ± 3 | 565 ± 2 | 11.4 ± 0.5 |
| 160 °C | 470 ± 4 | 556 ± 5 | 10.0 ± 1.2 |

**Table 3.** Mechanical properties of 7075-HCu subjected to different PA treatments.

| Aging Temp. | YS (MPa) | UTS (MPa) | Total Elongation (%) |
|---|---|---|---|
| 100 °C | 458 ± 2 | 596 ± 3 | 13.5 ± 1.3 |
| 120 °C | 551 ± 6 | 623 ± 9 | 11.3 ± 1.0 |
| 140 °C | 508 ± 5 | 587 ± 3 | 10.9 ± 0.9 |
| 160 °C | 490 ± 5 | 564 ± 6 | 11.6 ± 0.6 |

*3.3. TEM Images and Analysis*

In the TEM images taken along the $[110]_{Al}$ zone axes, $\eta'$ precipitates were observed to have two kinds of morphologies. As mentioned above, $\eta'$ precipitates in the edge-on configuration appear as thick lines, while those not in the edge-on configuration appear as ellipses. Moreover, $\eta'$ precipitates in the edge-on configurations intuitively present specific orientation relationships with one another, and their habit planes are indicated by white lines in Figures 4 and 5. Previous work on the investigation of Al-9.4Zn-2.5Mg-2.5Cu alloy [35] observed that $\eta'$ and $\eta_2$ are the dominant precipitates. In the present work, we randomly characterized precipitates in all the artificial aging conditions by HR-TEM and applied FFT to examine whether or not most of the precipitates were $\eta'$. After the examination of a considerable number (around 100) of nano-particles, our results suggested that most were indeed $\eta'$ precipitates. The representative HR-TEM images with the corresponding FFT diffractograms and simulated diffraction patterns are shown in Figure 6. Identifications of $\eta'$ phase via 0002 and 0004 diffraction spots are indicated by yellow arrows in Figure 6b–c and 6e–f for 7075-LCu samples, respectively, subjected to the PA conditions at 120 °C and 160 °C; under the observation of $[10\bar{1}0]_{\eta'} // [110]_{Al}$ zone axis, the orientation between $\eta'$ phase and the aluminum matrix can be illustrated in Figure 6c,f. Based on the findings, the nano-precipitates formed after aging processes in the present work were presumed to be the $\eta'$ phase, so statistical analysis was further carried out.
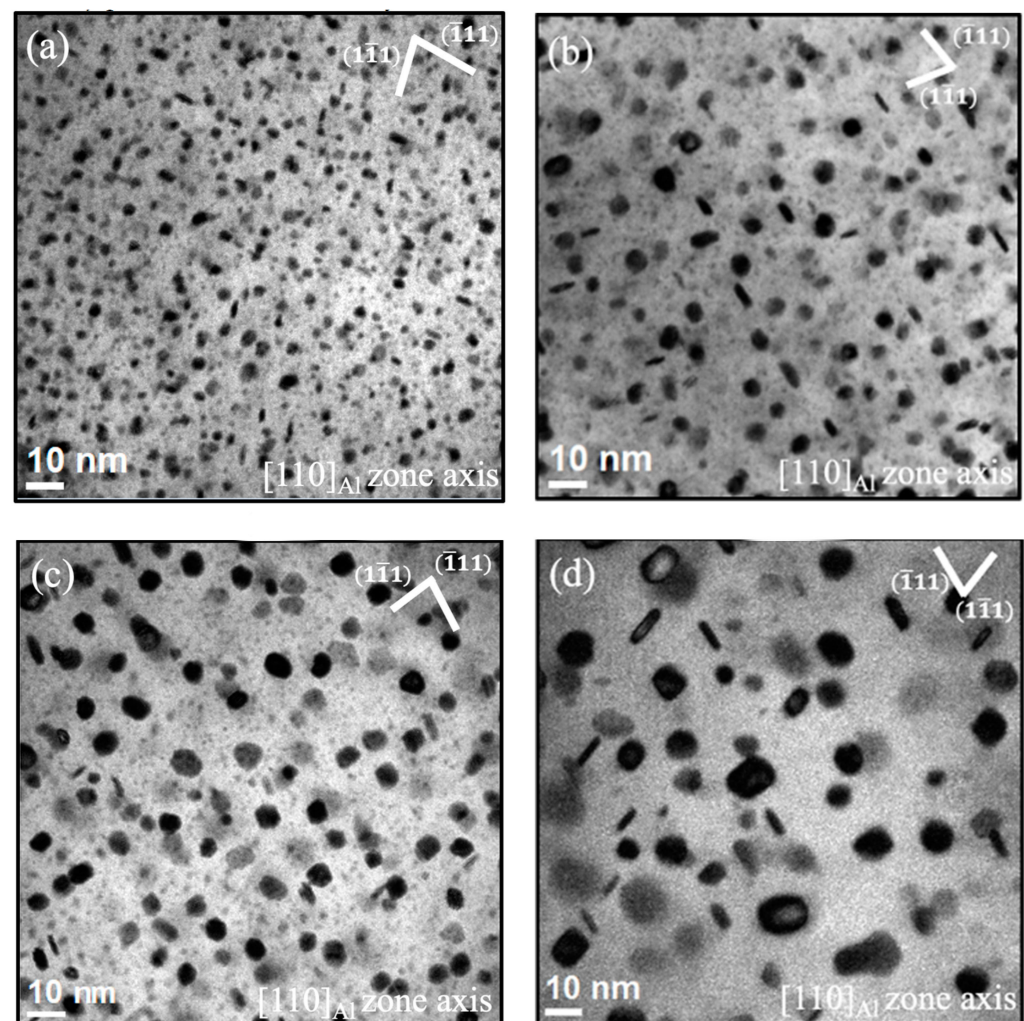


**Figure 4.** TEM images of $\eta'$ precipitates of 7075-LCu obtained from the PA conditions at (**a**) 100 °C, (**b**) 120 °C, (**c**) 140 °C, and (**d**) 160 °C.
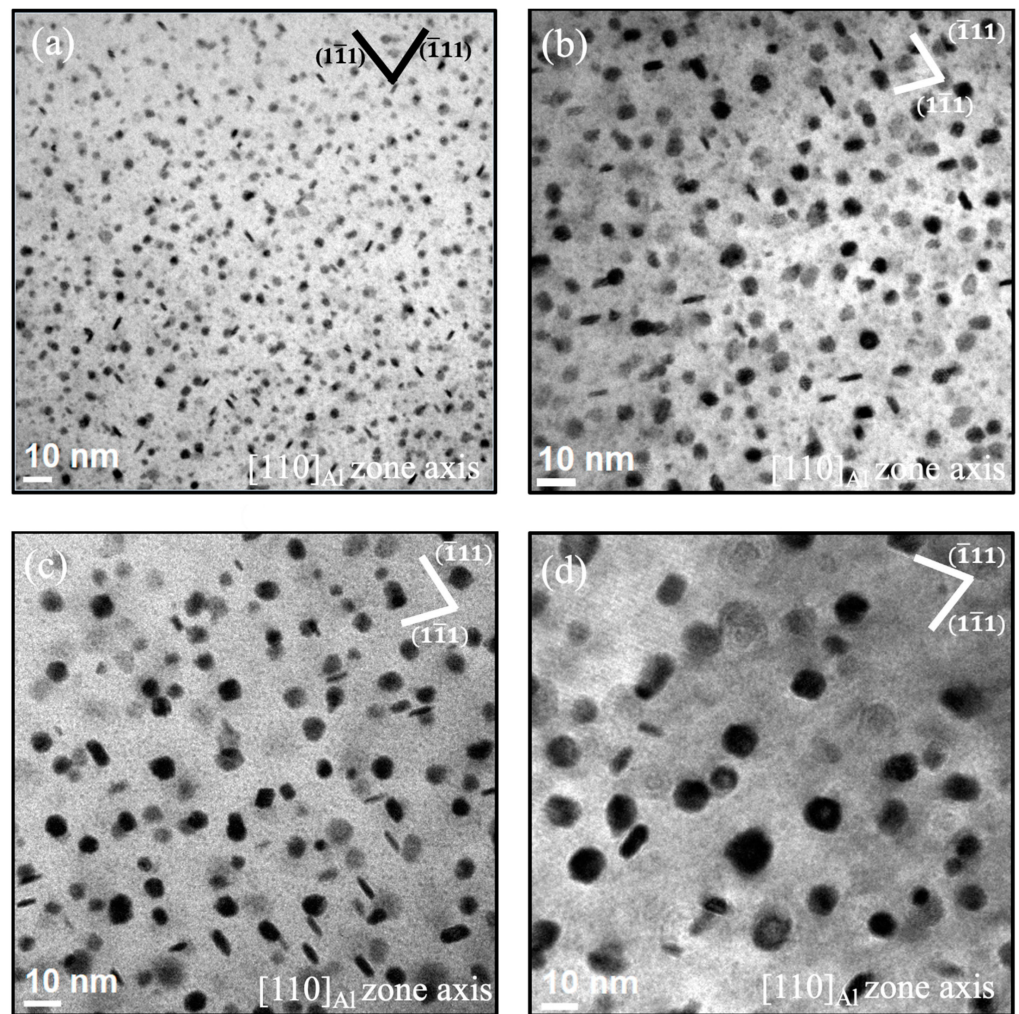
**Figure 5.** TEM images of η′ precipitates of 7075-HCu obtained from the PA conditions at (**a**)100 °C, (**b**) 120 °C, (**c**) 140 °C, and (**d**) 160 °C.
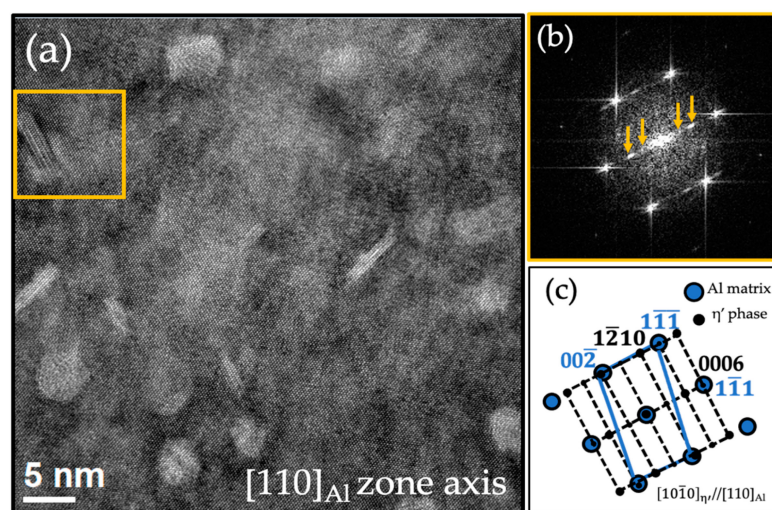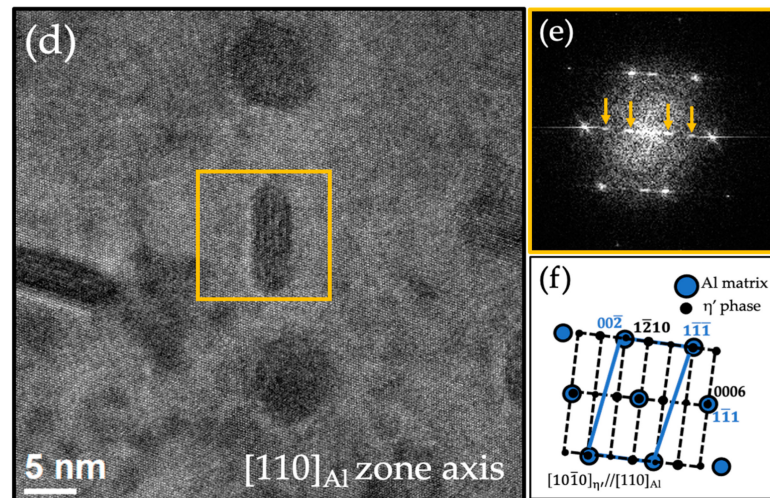


**Figure 6.** *Cont.*

**Figure 6.** HR-TEM images, FFT diffractograms, and corresponding simulated diffraction patterns of η′ precipitates of 7075-LCu obtained from the PA conditions at (**a–c**) 120 °C, and (**d–f**) 160 °C.

### 3.4. Effect of Cu on η′ Precipitates

Figure 7a presents a high-angle-annual dark field (HAADF) image of the 7075-LCu sample, which was treated by 120 °C PA condition, observed along the $[110]_{Al}$ zone axis. Two of the edge-on η′ precipitates are framed by red squares, showing Zn, which has a much higher Z (atomic number) than that of Al, to be the major component of η′ precipitates. From the EDX-mappings (Figure 7b–f), it can be seen that the corresponding bright regions on the HAADF images are also enriched regions of Zn and Mg. In contrast, the Al map shows depletions at the locations of η′ precipitates, while the Cu map shows no such depletions at those locations. This result implies that Cu could participate in the formation of η′ precipitates. Figure 7f more clearly shows that those Al-depleted regions are filled with Cu. Figure 8 presents the counterparts of the 7075-HCu sample to the 7075-LCu sample in the same PA condition, displaying a similar trend.
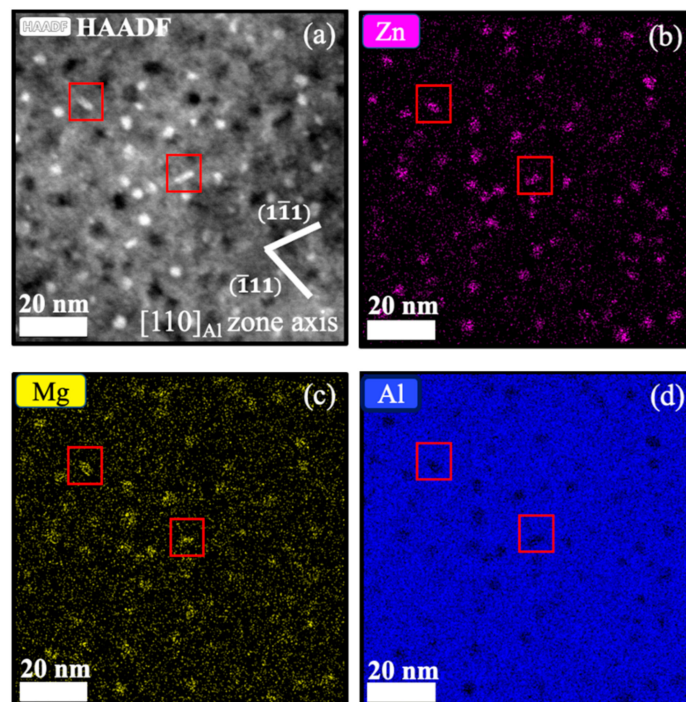


**Figure 7.** *Cont.*
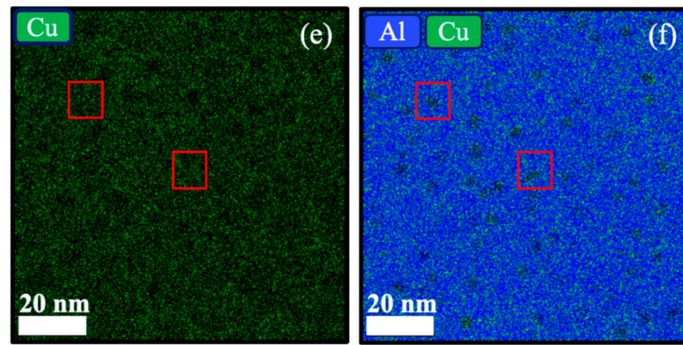
**Figure 7.** STEM-HAADF image with EDX mappings of η′ precipitates of 7075-LCu in the 120 °C PA condition: (**a**) STEM-HAADF image; (**b**–**e**) EDS maps of Zn, Mg, Al, and Cu; (**f**) overlapped Al and Cu maps. η′ precipitates were indicated by the red squares.



**Figure 8.** STEM-HAADF image with EDX mappings of η′ precipitates of 7075-HCu in the 120 °C PA condition: (**a**) STEM-HAADF image; (**b**–**e**) EDS maps of Zn, Mg, Al, and Cu; (**f**) overlapped Al and Cu maps. η′ precipitates were indicated by the red squares.
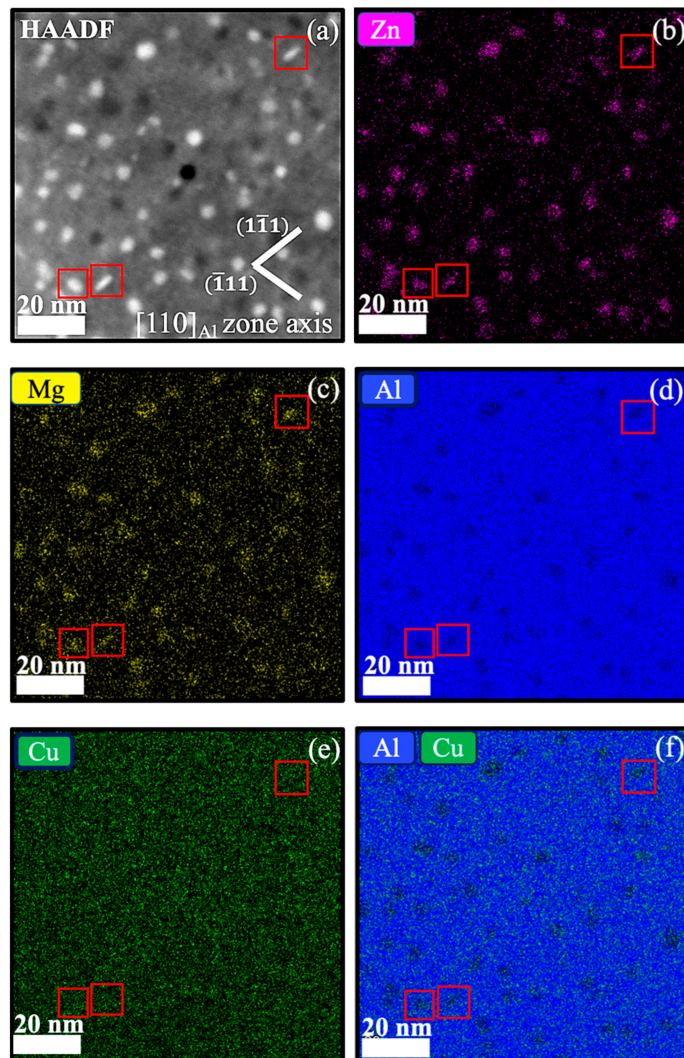
*3.5. Precipitate Size and Number Density Analysis*

η′ precipitates in the TEM images were further measured and statistically analyzed with the open-source software Fiji [28]. Figure 8a shows a TEM bright-field image, where

the precipitates are black and the Al matrix is white. The sharp images of the precipitates can be improved by tilting the matrix to slightly deviate from the $[110]_{Al}$ zone axis and finding specific regions in the matrix. Usually, these specific areas are slightly bent or distorted by the nearby secondary phases, so the regions slightly deviate from the exact zones. The deviation and the specific diffraction condition cause the Al matrix to be bright and the precipitates dark. To analyze the sizes of $\eta'$ precipitates, an $\eta'$ precipitate with an area larger than 2.56 nm$^2$ was chosen and marked in red. The boundary was set at 2.56 nm$^2$ based on a previous work [14] that discriminated the solute clusters and the precipitates, the latter having an effective radius of $\geq 1.00$ nm. Considering the projection effect, 2.56 nm$^2$/0.816 is about 3.14 nm$^2$ (a real area), which is equal to 3.14 nm$^2$ (effective radius = 1.00 nm), so it is reasonable to assume that 2.56 nm$^2$ is an appropriate lower bound to exclude both solute clusters and noises in the images. To prevent bias, the present work also excluded overlapped precipitates, which could not be discerned from one another, and precipitates at the edges of the frames. Moreover, unclearly projected precipitates were excluded to avoid bias and increase the effectiveness by allowing the software simultaneously to choose the regions above the assigned grayscale threshold. The chosen precipitates were further divided into two groups, the edge-on group and the non-edge-on group, according to their circularity; the precipitates in non-edge configurations with elliptical areas greater than 2.56 nm$^2$ were selected for size measurements.

Generally, since the edge-on precipitates appear as thick lines, they can be discriminated from other precipitates by their lower circularity (Figure 9a). After the precipitates were classified by their circularity, some exceptions needed to be included or excluded according to their morphologies and orientation relationships with the Al matrix. The schematic diagram shown in Figure 1c illustrates the presumed circular plate-like morphology of $\eta'$ (the thickness denoted as t, and the radius, r). The selected precipitates in the non-edge-on and edge-on groups were respectively marked blue and green, as shown in Figure 9b,c. In the former case, these ellipses did not present the actual area of the plate-like $\eta'$ and their true areas were estimated after dividing the areas of ellipses by the projection factor of 0.816 (i.e., cos 35.26°) as previously described. In the latter case, the real thickness was measured directly from the thick line morphology. We measured at least 300 precipitates from three grains for each condition. More than 300 precipitates in four TEM frames were employed in each statistical analysis. The average data of the true area (A), thickness (t), and volume (A × t) of $\eta'$ precipitate for 7075-LCu and 7075-HCu samples subjected to different PA conditions are respectively listed in Tables 4 and 5. The measured results showed that the $\eta'$ precipitates of 7075-LCu were slightly larger than those of 7075-HCu. For instance, at the 120 °C PA condition, the average thicknesses of the $\eta'$ precipitates were 2.15 nm (7075-LCu) and 2.04 nm (7075-HCu), respectively.
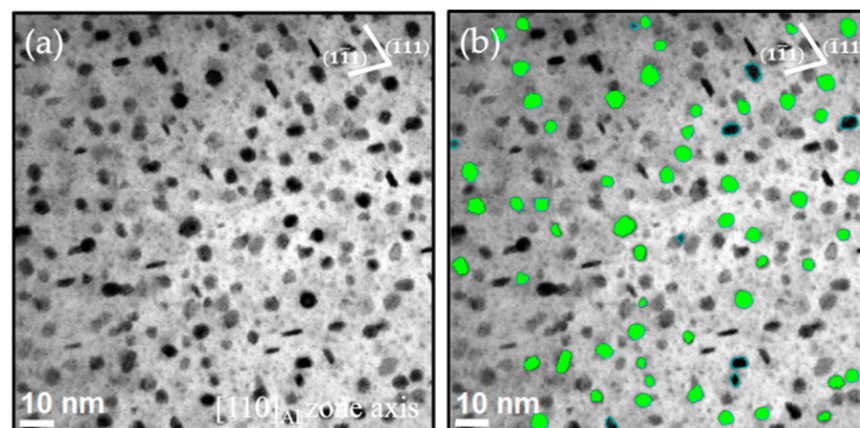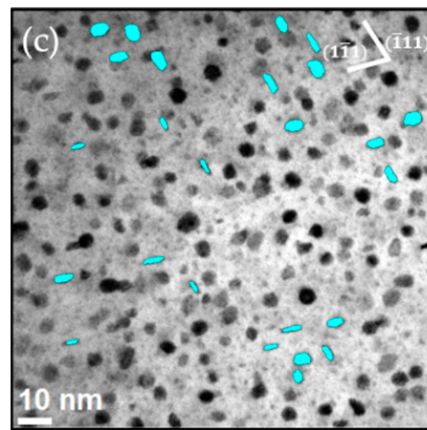


**Figure 9.** *Cont.*

**Figure 9.** Statistically analyzing η′ precipitate images of 7075-HCu subjected to 120 °C PA: (**a**) TEM image, (**b**) selected non-edge-on precipitates, and (**c**) selected edge-on precipitates.

**Table 4.** Average sizes of η′ precipitate of 7075-LCu subjected to different PA conditions.

| Aging Temp. | Area (nm$^2$) | Thickness (nm) | Volume (nm$^3$) |
|---|---|---|---|
| 100 °C | 8.34 ± 4.33 | 1.82 ± 0.42 | 15.2 |
| 120 °C | 18.2 ± 10.9 | 2.15 ± 0.63 | 39.1 |
| 140 °C | 36.0 ± 21.9 | 2.74 ± 1.12 | 98.6 |
| 160 °C | 95.6 ± 41.3 | 4.26 ± 1.52 | 407 |

**Table 5.** Average sizes of η′ precipitate of 7075-HCu subjected to different PA conditions.

| Aging Temp. | Area (nm$^2$) | Thickness (nm) | Volume (nm$^3$) |
|---|---|---|---|
| 100 °C | 7.66 ± 3.78 | 1.59 ± 0.40 | 12.2 |
| 120 °C | 15.3 ± 6.83 | 2.03 ± 0.65 | 31.1 |
| 140 °C | 28.2 ± 13.5 | 2.39 ± 1.09 | 67.4 |
| 160 °C | 86.9 ± 45.2 | 3.87 ± 1.21 | 336 |

Furthermore, the measured number densities (per unit volume) for all PA conditions are presented in Tables 6 and 7. For each condition, number density measurements were performed on at least three different grains. Volume percent was obtained by the multiple of the single precipitate volume and the number density. The result shows the number density decreased with increasing the volume percent as the temperature of PA increased. Since a small number of precipitates could be too blurred to be distinguished, there could be a slight underestimation of the number density and volume percent; the precipitates at 100 °C PA have the smallest average size and are therefore likely the most underestimated. However, the decreasing trend of the number density is still manifested with the increase of PA temperature.

**Table 6.** Number density and volume percent of 7075-LCu subjected to different PA conditions.

| 7075-LCu | 100 °C PA | 120 °C PA | 140 °C PA | 160 °C PA |
|---|---|---|---|---|
| Number density (cm$^{-3}$) | $4.22 \times 10^{17}$ | $3.27 \times 10^{17}$ | $1.97 \times 10^{17}$ | $8.72 \times 10^{16}$ |
| Volume percent | 0.641% | 1.28% | 1.94% | 3.54% |

**Table 7.** Number density and volume percent of 7075-HCu subjected to different PA conditions.

| 7075-HCu | 100 °C PA | 120 °C PA | 140 °C PA | 160 °C PA |
|---|---|---|---|---|
| Number density (cm$^{-3}$) | $4.58 \times 10^{17}$ | $3.52 \times 10^{17}$ | $2.26 \times 10^{17}$ | $1.02 \times 10^{17}$ |
| Volume percent | 0.559% | 1.09% | 1.52% | 3.42% |

Figure 10 presents the plot of number density versus aging temperature for the two alloys subjected to different PA conditions. Both 7075-HCu and 7075-LCu samples demonstrated that the particle density decreased with increasing the aging temperature; at the same aging temperature, the former possessed a higher number density of η′ precipitates than the latter. Figure 11 displays that the average thickness and average area are a function of aging temperature for the two alloys subjected to different PA conditions. Both 7075-HCu and 7075-LCu samples display that the average thickness and average area increase with increasing the aging temperature; at the same aging temperature the former had a smaller size as compared to the latter.
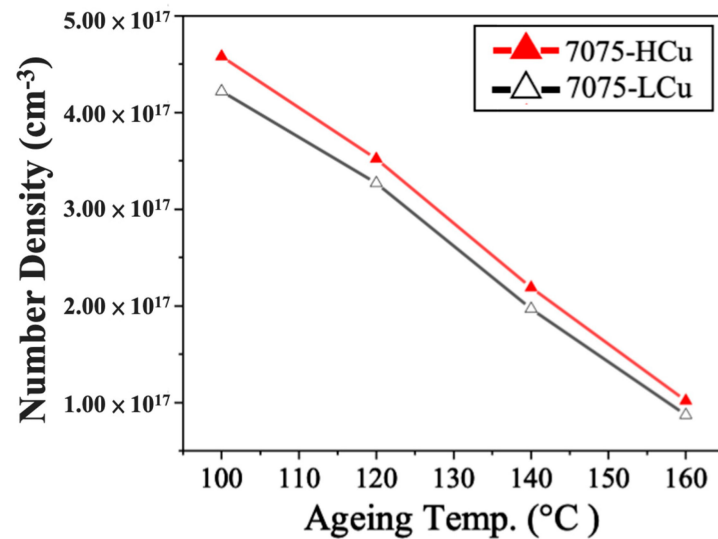


**Figure 10.** Plot of number density of precipitate versus aging temperature for the two alloys subjected to different PA conditions.
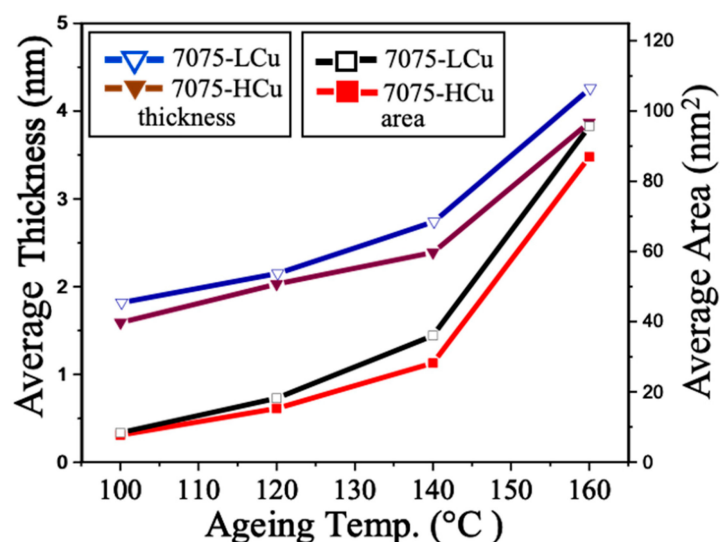


**Figure 11.** Plot of average area and average thickness of precipitate versus aging temperature for the two alloys subjected to different PA conditions.

Previous research works [8,36] claimed that the average size of η′ precipitates mainly influences the mechanical properties. Our results demonstrated that at the 120 °C PA condition, both alloys had the optimal UTS strengths, 618 MPa (7075-LCu) and 623 MPa (7075-HCu), and the former possessed the average thicknesses of η′ precipitates (2.15 nm) with a number density ($3.27 \times 10^{17}$ cm$^{-3}$); the latter, 2.04 nm, and $3.52 \times 10^{17}$ cm$^{-3}$.

Previous work on a series of Al-Zn-Mg-Cu alloys [36] has also suggested that the critical value of the size of the η′ precipitate for the optimal peak hardening is about 2 nm, which is close to our experimental results.

## 4. Conclusions

In the present work, two 7075 alloys, 5.98Zn-2.86Mg-1.61Cu and Al-5.91Zn-2.83Mg-1.98Cu (wt.%), with the same base composition but different contents of Cu (1.61 and 1.98 wt.%), respectively denoted as 7075-LCu and 7075-HCu, have been investigated. The aging treatments at various temperatures (100,120, 140, and 160 °C) with different holding times of up to 24 h were conducted. For both alloys, the highest strength can be achieved by 120 °C/24 h artificial aging. The UTS in such conditions achieved 618 MPa (7075-LCu) and 623 MPa (7075-HCu). The crystallography and orientation relationships between η′ and the Al matrix have been illustrated. η′ precipitates grow on their habit planes, $\{111\}_{Al}$, with four variants. Under TEM observation along the $[110]_{Al}$ zone axis, only two of four η′ variants can be edge-on and appear to be thick lines; the other two non-edge-on variants of η′ would be projected as ellipses. A method for measuring the sizes of numerous η′ precipitates has been developed. The average data of the thickness, true area, and volume of η′ platelets were calculated. Subsequently, the number density and the volume fraction of the η′ precipitates were estimated. The correlation of the UTS to η′ precipitate size (thickness and true area) and number density was linked. It was found that when the 7075-LCu and 7075-HCu samples had the highest UTS strengths, which were related to the finer size and higher number density of the η′ precipitates; the former possessed an average thickness of 2.15 nm, and a number density of $3.27 \times 10^{17}$ cm$^{-3}$; the latter, 2.04 nm, and $3.52 \times 10^{17}$ cm$^{-3}$.

**Author Contributions:** Conceptualization, T.-J.H. and J.-R.Y.; investigation, T.-J.H., P.-H.C., C.-L.T., T.-C.T., C.-Y.T., Y.-X.L., H.-R.C., T.-F.C., C.-Y.C. and S.-H.W.; supervision, J.-R.Y.; writing—original draft, T.-J.H. All authors have read and agreed to the published version of the manuscript.

**Institutional Review Board Statement:** Not applicable.

**Informed Consent Statement:** Not applicable.

**Data Availability Statement:** The data presented in this study are available on request from the corresponding author.

**Conflicts of Interest:** The authors declare that they have no known competing financial interests or personal relationships that could have appeared to influence the work reported in this paper.

## References

1. Li, X.Z.; Hansen, V.; Gjonnes, J.; Wallenberg, L.R. HREM study and structure modeling of the eta η′ phase, the hardening precipitates in commercial Al-Zn-Mg alloys. *Acta Mater.* **1999**, *47*, 2651–2659. [CrossRef]
2. Sha, G.; Cerezo, A. Early-stage precipitation in Al-Zn-Mg-Cu alloy (7050). *Acta Mater.* **2004**, *52*, 4503–4516. [CrossRef]
3. Wen, K.; Fan, Y.Q.; Wang, G.J.; Jin, L.B.; Li, X.W.; Li, Z.H.; Zhang, Y.G.; Xiong, B.Q. Aging behavior and precipitate characterization of a high Zn-containing Al-Zn-Mg-Cu alloy with various tempers. *Mater. Des.* **2016**, *101*, 16–23. [CrossRef]
4. Li, X.W.; Xiong, B.Q.; Zhang, Y.A.; Hua, C.; Wang, F.; Zhu, B.H.; Liu, H.W. Effect of one-step aging on microstructure and properties of a novel Al-Zn-Mg-Cu-Zr alloy. *Sci. China Ser. E-Technol. Sci.* **2009**, *52*, 67–71. [CrossRef]
5. Fan, X.; Jiang, D.; Meng, Q.; Lai, Z.; Zhang, X. Characterization of precipitation microstructure and properties of 7150 aluminium alloy. *Mater. Sci. Eng. A* **2006**, *427*, 130–135. [CrossRef]
6. Luo, J.; Luo, H.Y.; Li, S.J.; Wang, R.Z.; Ma, Y. Effect of pre-ageing treatment on second nucleating of GPII zones and precipitation kinetics in an ultrafine grained 7075 aluminum alloy. *Mater. Des.* **2020**, *187*, 14. [CrossRef]
7. Ghosh, A.; Ghosh, M.; Shankar, G. On the role of precipitates in controlling microstructure and mechanical properties of Ag and Sn added 7075 alloys during artificial ageing. *Mater. Sci. Eng. A* **2018**, *738*, 399–411. [CrossRef]

8. Zhao, Y.X.; Li, H.; Liu, Y.; Huang, Y.C. The microstructures and mechanical properties of a highly alloyed Al-Zn-Mg-Cu alloy: The role of Cu concentration. *J. Mater. Res. Technol.* **2022**, *18*, 122–137. [CrossRef]

9. Ghiaasiaan, R.; Amirkhiz, B.S.; Shankar, S. Quantitative metallography of precipitating and secondary phases after strengthening treatment of net shaped casting of Al-Zn-Mg-Cu (7000) alloys. *Mater. Sci. Eng. A* **2017**, *698*, 206–217. [CrossRef]

10. Liu, D.M.; Xiong, B.Q.; Bian, F.G.; Li, Z.H.; Li, X.W.; Zhang, Y.G.; Wang, F.; Liu, H.W. Quantitative study of precipitates in an Al-Zn-Mg-Cu alloy aged with various typical tempers. *Mater. Sci. Eng. A* **2013**, *588*, 1–6. [CrossRef]

11. Liu, D.M.; Xiong, B.Q.; Bian, F.G.; Li, Z.H.; Li, X.W.; Zhang, Y.G.; Wang, Q.S.; Xie, G.L.; Wang, F.; Liu, H.W. Quantitative study of nanoscale precipitates in Al-Zn-Mg-Cu alloys with different chemical compositions. *Mater. Sci. Eng. A.* **2015**, *639*, 245–251. [CrossRef]

12. Azarniya, A.; Taheri, A.K.; Taheri, K.K. Recent advances in ageing of 7xxx series aluminum alloys: A physical metallurgy perspective. *J. Alloys Compd.* **2019**, *781*, 945–983. [CrossRef]

13. Liu, J.Z.; Hu, R.; Zheng, J.L.; Zhang, Y.D.; Ding, Z.G.; Liu, W.; Zhu, Y.T.; Sha, G. Formation of solute nanostructures in an Al-Zn-Mg alloy during long-term natural aging. *J. Alloys Compd.* **2020**, *821*, 10. [CrossRef]

14. Geng, Y.X.; Song, Q.; Zhang, Z.R.; Pan, Y.L.; Li, H.X.; Wu, Y.; Zhu, H.H.; Zhang, D.; Zhang, J.S.; Zhuang, L.Z. Quantifying early-stage precipitation strengthening of Al-Mg-Zn(-Cu) alloy by using particle size distribution. *Mater. Sci. Eng. A.* **2022**, *839*, 13. [CrossRef]

15. Matsuda, K.; Yasumoto, T.; Bendo, A.; Tsuchiya, T.; Lee, S.; Nishimura, K.; Nunomura, N.; Marioara, C.D.; Levik, A.; Holmestad, R.; et al. Effect of Copper Addition on Precipitation Behavior near Grain Boundary in Al-Zn-Mg Alloy. *Mater. Trans.* **2019**, *60*, 1688–1696. [CrossRef]

16. Shu, W.X.; Hou, L.G.; Zhang, C.; Zhang, F.; Liu, J.C.; Liu, J.T.; Zhuang, L.Z.; Zhang, J.S. Tailored Mg and Cu contents affecting the microstructures and mechanical properties of high-strength Al-Zn-Mg-Cu alloys. *Mater. Sci. Eng. A.* **2016**, *657*, 269–283. [CrossRef]

17. Chung, T.F.; Yang, Y.L.; Huang, B.M.; Shi, Z.S.; Lin, J.G.; Ohmura, T.; Yang, J.R. Transmission electron microscopy investigation of separated nucleation and in-situ nucleation in AA7050 aluminium alloy. *Acta Mater.* **2018**, *149*, 377–387. [CrossRef]

18. Berg, L.K.; Gjonnes, J.; Hansen, V.; Li, X.Z.; Knutson-Wedel, M.; Waterloo, G.; Schryvers, D.; Wallenberg, L.R. GP-zones in Al-Zn-Mg alloys and their role in artificial aging. *Acta Mater.* **2001**, *49*, 3443–3451. [CrossRef]

19. Gjonnes, J.; Simensen, C.J. An electron microscope investigation of microstructure in an aluminum-zinc-magnesium alloy. *Acta Metall.* **1970**, *18*, 881. [CrossRef]

20. Auld, J.H.; Cousland, S.M. Structure of the metastable eta prime phase in aluminium-zinc magnesium alloys. *J. Aust. Inst. Met.* **1974**, *19*, 194–199.

21. Zhao, P.H.; Wu, X.L.; Gao, K.Y.; Wen, S.P.; Rong, L.; Huang, H.; Wei, W.; Nie, Z.R. Effect of Zn/Mg ratio on microstructure and mechanical properties of Al-Zn-Mg alloys. *Mater. Lett.* **2022**, *312*, 4. [CrossRef]

22. Lin, Y.-R.; Chen, W.-Y.; Tan, L.; Hoelzer, D.T.; Yan, Z.; Hsieh, C.-Y.; Huang, C.-W.; Zinkle, S.J. Bubble formation in helium-implanted nanostructured ferritic alloys at elevated temperatures. *Acta Mater.* **2021**, *217*, 117165. [CrossRef]

23. Lozano-Perez, S.; Sha, G.; Titchmarsh, J.M.; Jenkins, M.L.; Hirosawa, S.; Cerezo, A.; Smith, G.D.W. Comparison of the number densities of nanosized Cu-rich precipitates in ferritic alloys measured using EELS and EDX mapping, HREM and 3DAP. *J. Mater. Sci.* **2006**, *41*, 2559–2565. [CrossRef]

24. Liao, Y.G.; Han, X.Q.; Zeng, M.X.; Jin, M. Influence of Cu on microstructure and tensile properties of 7XXX series aluminum alloy. *Mater. Des.* **2015**, *66*, 581–586. [CrossRef]

25. Pengxuan Dong, S.C. Kanghua Chen, Effects of Cu content on microstructure and properties of super-high-strength Al-9.3Zn-2.4Mg-xCu-Zr alloy. *J. Alloys Compd.* **2019**, *788*, 9.

26. Fang, X.; Du, Y.; Song, M.; Li, K.; Jiang, C. Effects of Cu content on the precipitation process of Al-Zn-Mg alloys. *J. Mater. Sci.* **2012**, *47*, 8174–8187. [CrossRef]

27. Chung, T.F.; Kawasaki, M.; Wang, P.; Nishio, K.; Shiojiri, M.; Li, W.C.; Hsiao, C.N.; Yang, J.R. Atomic-resolution energy dispersive X-ray spectroscopy mapping of eta precipitates in an Al-Mg-Zn-Cu alloy. *Mater. Charact.* **2020**, *166*, 8. [CrossRef]

28. Schindelin, J.; Arganda-Carreras, I.; Frise, E.; Kaynig, V.; Longair, M.; Pietzsch, T.; Preibisch, S.; Rueden, C.; Saalfeld, S.; Schmid, B.; et al. Fiji: An open-source platform for biological-image analysis. *Nat Methods.* **2012**, *9*, 676–682. [CrossRef]

29. Wolverton, C. Crystal structure and stability of complex precipitate phases in Al–Cu–Mg–(Si) and Al–Zn–Mg alloys. *Acta Mater.* **2001**, *49*, 3129–3142. [CrossRef]

30. Iakoubovskii, K.; Mitsuishi, K.; Nakayama, Y.; Furuya, K. Thickness measurements with electron energy loss spectroscopy. *Microsc. Res. Tech.* **2008**, *71*, 626–631. [CrossRef]

31. Malis, T.; Cheng, S.C.; Egerton, R.F. EELS log-ratio technique for specimen-thickness measurement in the TEM. *J.Electron Microsc. Tech.* **1988**, *8*, 193–200. [CrossRef] [PubMed]

32. Zhang, H.-R.; Egerton, R.F.; Malac, M. Local thickness measurement through scattering contrast and electron energy-loss spectroscopy. *Micron* **2012**, *43*, 8–15. [CrossRef] [PubMed]

33. Loffler, H.; Kovacs, I.; Lendvai, J. Decomposition processes in al-zn-mg alloys. *J. Mater. Sci.* **1983**, *18*, 2215–2240. [CrossRef]

34. Wagner, R.; Kampmann, R.; Voorhees, P.W. Homogeneous second-phase precipitation. In *Chapter 5 in Phase Transformations in Materials*; Kostorz, G., Ed.; WILEY-VCH Verlag GmbH: Weinheim, Germany, 2001.

35. Sha, G.; Wang, Y.B.; Liao, X.Z.; Duan, Z.C.; Ringer, S.P.; Langdon, T.G. Influence of equal-channel angular pressing on precipitation in an Al-Zn-Mg-Cu alloy. *Acta Mater.* **2009**, *57*, 3123–3132. [CrossRef]

36. Zou, Y.; Wu, X.; Tang, S.; Zhu, Q.; Song, H.; Guo, M.; Cao, L. Investigation on microstructure and mechanical properties of Al-Zn-Mg-Cu alloys with various Zn/Mg ratios. *J. Mater. Sci. Technol.* **2021**, *85*, 106–117. [CrossRef]